Surface Layer Turbulence Measurements during a Frontal Passage

M. PIPER*

Program in Atmospheric and Oceanic Sciences, University of Colorado, Boulder, Colorado

JULIE K. LUNDQUIST

Atmospheric Science Division, Lawrence Livermore National Laboratory, Livermore, California

(Manuscript received 21 January 2004, in final form 2 March 2004)

ABSTRACT

Very little is known about the nature of turbulence in the transition zone of a synoptic-scale cold front, especially at the dissipative scales. Lacking this knowledge, accurate models of surface frontogenesis are compromised. To address this problem, high-frequency measurements from sonic and hot-wire anemometers are used to analyze the finescale turbulence in the atmospheric surface layer (ASL) within a cold front observed in the MICROFRONTS field experiment. To quantify the turbulence in the front, velocity spectra and dissipation rates are calculated as functions of time and stability in the ASL. The normalized first and second moments of the one-dimensional velocity spectrum conform to the scaling suggested by Kolmogorov's equilibrium hypotheses, even during the intense turbulence associated with the frontal passage. The spectra compare well with other data collected at high Re_λ in the ASL, but not as well with a recent model of the dissipative range of turbulence. Dissipation rate ϵ is calculated with one direct and two indirect techniques. The calculations from the different techniques compare well with one another and, when nondimensionalized, with a historical expression for dissipation rate as a function of ASL stability. The magnitude of the dissipation rate increases by an order of magnitude to a maximum value of $\sim 1.2\ \mathrm{m^2\ s^{-3}}$ during the frontal passage compared to prefrontal values of $\sim 0.05\ \mathrm{m^2\ s^{-3}}$; the latter is typical for a slightly stable nighttime boundary layer over land. These results can be used in assessing the effects of turbulence in traditional semigeostrophic models of frontal collapse. The dissipation rate calculations may be of particular use to modelers.

1. Introduction

What physical mechanism counteracts the intensification of temperature and velocity gradients across a developing front? Emanuel (1985) offers two current schools of thought on the subject: 1) a minimum cross-frontal scale may be reached when frontogenetical forcing is balanced by turbulent mixing and dissipation within the frontal zone (Hoskins and Bretherton 1972; Williams 1974), or 2) as advanced by Orlanski and Ross (1984) and Orlanski et al. (1985), numerical simulations employing the primitive equations suggest that frontal zone contraction may be limited by ageostrophic motions that develop at the frontal boundary and reduce vorticity generation. However, these numerical simulations, which have been extended, for example, by Gall et al. (1987), Garner (1989), and Snyder et al. (1993), show that in the absence of dissipation, frontal collapse proceeds to the grid size of the simulation, which may be at scales as small as *O*(km). The key missing ingredient for these studies appears to be actual measurements of turbulence in a frontal zone.

A survey of the literature reveals that there have been studies of turbulence in the boundary layer during frontal passages (Young and Johnson 1984; Shapiro 1984; Shapiro et al. 1985; Taylor et al. 1993); however, these investigations are focused more on describing the mean vertical structure and circulation in the boundary layer during a frontal passage. Very little is said about the characteristics of turbulence at small time scales and high wavenumbers during these frontal passages.

Some recent investigations have begun to quantify turbulence and dissipation in frontal zones. Frank (1994) examines the turbulence structure of two fronts that passed a 200-m instrumented tower near Karlsruhe, Germany. In addition to showing the mean vertical structure of the fronts as they pass the tower, Frank demonstrates that there is an order of magnitude or more increase in turbulent kinetic energy across the frontal zone. Blumen and Piper (1999) reported turbulence statistics, including dissipation rate measurements, from the MICRO-

* On leave from Research Systems, Inc., Boulder, Colorado.

Corresponding author address: Julie K. Lundquist, Atmospheric Science Division, L-103, Lawrence Livermore National Laboratory, Livermore, CA 94551.
E-mail: jkl@llnl.gov

TABLE 1. Turbulence instrumentation on the ASTER towers in MICROFRONTS.

Instrument	Manufacturer and model number	Location (m)	Variables	Sampling rate (samples per second)
Sonic anemometer	ATI K-probe	3, 10 S	u, v, w, T_v	10
Hot-wire anemometer	TSI 1210	3 S	s	9600
Prop-vane anemometer	R.M. Young 35005	3, 5, 10 S	u, v	5
Resistance thermometer	AIR, Inc.	3, 10 S	T	20
UV hygrometer	CSI	3, 10 S	ρ_v	20
T/RH sensor	NCAR/Väisälä	2, 3, 5, 7, 10 S	T, RH	0.5
Sonic anemometer	Gill	10 N	u, v, w, T_v	21
Prop-vane anemometer	R.M. Young 35005	3, 5, 10 N	u, v	5
Resistance thermometer	AIR, Inc.	10 N	T	20
T/RH sensor	NCAR/Väisälä	3, 10 N	T, RH	0.5

FRONTS field experiment, where high-frequency turbulence data were collected from tower-mounted hot-wire and sonic anemometers in a cold front and in a density current. Chapman and Browning (2001) measured dissipation rate in a precipitating frontal zone with high-resolution Doppler radar. Their measurements were conducted above the surface layer to heights of 5 km. The dissipation rate values they found are comparable to those measured in Kennedy and Shapiro (1975) in an upper-level front.

Here, we hope to expand on these recent studies by depicting the behavior of the fine scales of turbulence near the surface in a frontal zone. The primary objective of this study is to quantify the levels of turbulence and dissipation occurring in a frontal zone through the calculation of kinetic energy spectra and dissipation rates. The high-resolution turbulence data used in this study are taken during the cold front that passed the MICROFRONTS site in the early evening hours of 20 March 1995. These new measurements can be used as a basis for parameterizing the effects of surface layer turbulence in numerical models of frontogenesis.

An overview of the MICROFRONTS field experiment, as well as a description of the data collected in the front observed in this experiment, are provided in section 2. Section 2 also describes some of the data processing methods used, including a test for isotropy performed with the sonic anemometers and the in situ calibration of the hot-wire anemometer data. In section 3, one-dimensional kinetic energy spectra are presented as functions of time at intervals before, during, and after the frontal passage. When these spectra are made dimensionless with Kolmogorov scales, they appear to collapse, within error bounds, to a single function of dimensionless wavenumber. This dimensionless spectrum function compares favorably, even during the frontal passage, with that provided by Champagne (1978, Fig. 22 and curve fit in his Table 4). The spectra are also compared with a recent theoretical model of the equilibrium range of turbulence proposed by Pope (2000). It is found that the calculated spectra agree fairly well with Pope's model in the inertial subrange of turbulence, but not as well in the dissipative range. In section 4, three techniques for calculating the dissipation rate ϵ are presented: direct dissipation, inertial dissipation, and Kolmogorov's four-fifths law. Dissipation rate calculations using these techniques are employed using data from both the sonic and hot-wire anemometers, when possible. Unfortunately, direct calculations of ϵ were not possible during the frontal passage because the high wind speeds concurrent with the frontal passage demand very high-frequency resolution, beyond that possible with the hot-wire anemometer, for direct ϵ calculations. The calculations resulting from these three techniques are presented for the cold front, both as time series and as a dimensionless function of stability in the surface layer. Quantitative comparisons of the direct and indirect calculation techniques are also given. A summary and some suggestions for future work are given in section 5.

2. Data sources

a. Instrumentation and data preparation

The MICROFRONTS field experiment was conducted from 1 March 1995 through 30 March 1995 at a site near De Graff, Kansas approximately 75 km northeast of Wichita. The field site was situated in gently rolling farmland in eastern Kansas, with a homogeneous fetch to the northwest. The Atmosphere–Surface Turbulent Exchange Research (ASTER) facility, operated by the National Center for Atmospheric Research (NCAR) Atmospheric Technology Division, was deployed at MICROFRONTS to collect turbulence data. The ASTER setup consisted of two 10-m-tower groups, separated by 300 m along a southwest–northeast line, with turbulence instrumentation mounted at several levels, as shown in Table 1. In addition to the standard instrumentation in ASTER, a constant-temperature hot-wire anemometer was deployed at 3 m on the south tower to make fine-scale wind measurements and to directly measure dissipation rate ϵ. This hot wire, a TSI model 1210-T1.5 with a 1.3-mm-long, 4-μm-diameter tungsten wire, was oriented vertically to measure the horizontal component of the wind, and aligned at 315° from north to coincide with the climatologically preferred direction of frontal passages at the site.

The ASTER sonic anemometers on the south tower were used to compute turbulence statistics for the three

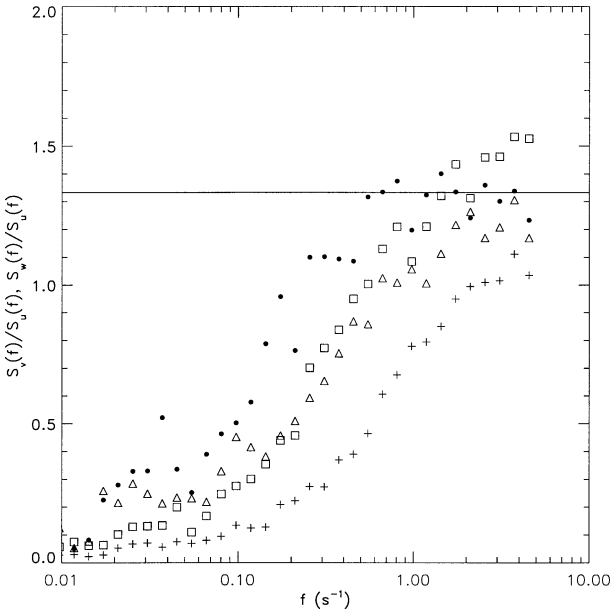

FIG. 1. A plot of the ratios between the v and u spectra and the w and u spectra showing the approach to the 4:3 ratio required by isotropy. Data are from the sonic anemometers at 3 and 10 m. Dots (●) denote S_v/S_u at 10 m, squares (□) S_w/S_u at 10 m, triangles (△) S_v/S_u at 3 m, and plus signs (+) S_w/S_u at 3 m.

velocity components. The data from the sonic anemometers are important not only because they can be used to calculate dissipation rate, but also because they can be used to demonstrate some evidence of local isotropy, which is necessary to justify the one-dimensional ϵ measurements from the hot-wire anemometer.

According to Champagne (1978), the existence of a $-5/3$ slope in a velocity spectrum is a relatively weak indicator of local isotropy. A stronger statement of isotropy and the existence of an inertial subrange is given by the 4:3 ratio between the amplitudes of the transverse (v)-to-streamwise (u) and the normal (w)-to-streamwise (u) component spectra (S) within inertial subrange frequencies. Figure 1 shows the ratio between the v and u spectra and the w and u spectra at 3 and 10 m for an hour of 10 samples per second data beginning at 0000 UTC 20 March 1995, about 2.5 h before the frontal passage. The surface layer was slightly stable during this period. In this case, the 10-m data approach and achieve the isotropic 4:3 ratio near $f = 1$ Hz. The value of S_v/S_u at 3 m almost achieves the 4:3 ratio before the Nyquist frequency at 5 Hz. The S_w/S_u ratio does not achieve the 4:3 ratio within the bandwidth of the sonic anemometer indicating that, at 3 m, the turbulence might still be feeling the effects of the ground. Kaimal (1986) suggests that the lowest height at which a sonic anemometer can be operated without subjecting the inertial subrange to flow distortion is $z_{\min} = 8\pi d \approx 3.8$ m for a path length $d = 15$ cm. This figure, which compares well with Kaimal et al. (1972, Fig. 22), suggests that an inertial subrange probably exists within frequencies measured by the sonic anemometer at 10 m, but its existence might be questionable in the frequency range of the sonic anemometer at 3 m.

Owing to the long run times of the hot wire in the MICROFRONTS experiment (continuous operation for several days), an in situ calibration of the hot-wire anemometer using wind speed data from the collocated sonic anemometer at 3 m was needed. The calibration was performed using King's law

$$E^2 = a + bU^n \tag{1}$$

(Hinze 1975; Bruun 1995), where E is hot-wire voltage, U is the wind speed, a and b are empirical coefficients to be determined, and $n = 0.45$ provides a good fit over the range of Reynolds numbers normally encountered in surface layer turbulence (Friehe 1986). Wind speeds from the 3-m sonic anemometer and the 9600 sample per second hot-wire anemometer voltages were block averaged into nonoverlapping 5-s intervals. A linear least squares fit was performed on (1), using 5-min blocks of the 5-s average E^2 and $U^{0.45}$ values, resulting in 5-min-average values of the coefficients a and b. King's law (1) can then be inverted to obtain wind speeds from the hot-wire anemometer. This technique was successfully used by Oncley et al. (1996) and as a check on the hot wires used by Champagne (1978).

For direct dissipation calculations, all scales that experience dissipation must be resolved. These scales include eddies at the Kolmogorov microscale η, which is given by

$$\eta = (\nu^3/\epsilon)^{1/4}, \tag{2}$$

where ν is kinematic molecular viscosity. During the frontal passage, η reached a minimum value of approximately 0.25 mm. The frequency required to resolve eddies on that scale, also known as the Kolmogorov frequency,

$$f_K = \frac{U}{2\pi\eta} \tag{3}$$

(Champagne 1978), is a function both of the Kolmogorov microscale and wind speed U. As wind speeds during the frontal passage reached 12 m s^{-1}, the Kolmogorov frequency $f_K = 7600$ Hz exceeded the Nyquist frequency of 4800 Hz for the hot wire. Therefore, not all scales experiencing dissipation during the frontal passage could be resolved. A rough guideline for the highest wind speeds that can be used for direct dissipation calculations with this hot-wire anemometer can be found by inverting (3) for $f_K = 4800$ Hz. The highest wind speed that allows resolution of a Kolmogorov microscale of 0.25 mm with a hot-wire anemometer sampling at 9600 Hz is about 7 m s^{-1}. This threshold is noted on the first panel of Fig. 2 to emphasize that direct dissipation calculations are inaccurate for wind speeds exceeding this threshold.

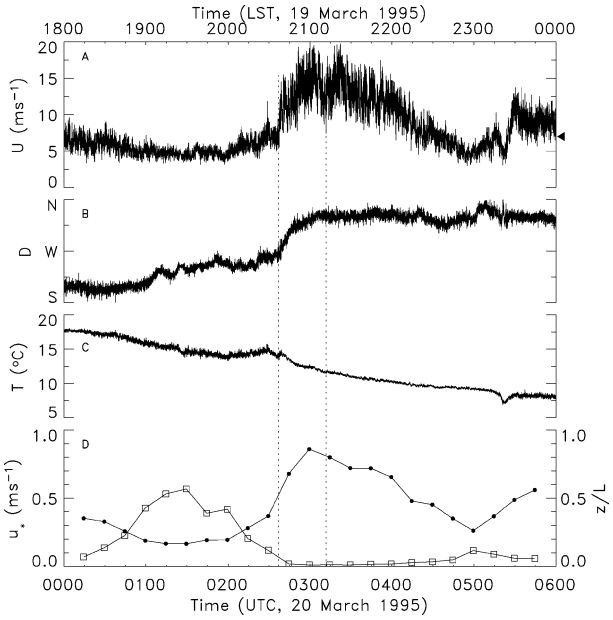

FIG. 2. Time series from the 10-m south tower instruments on 20 Mar 1995. (a) Wind speed from the sonic anemometer. The arrowhead on the right marks 7 m s^{-1}, the threshold for the hot-wire anemometer to resolve the Kolmogorov microscale η. (b) Wind direction from the sonic anemometer. (c) Temperature from the platinum resistance thermometer. (d) The friction velocity u_* (●) and the Monin–Obukhov scaling parameter $\zeta = z/L$ (□). The dotted lines give the extent of the frontal zone.

b. The cold front

A dry Arctic cold front passed the MICROFRONTS site at approximately 0237 UTC (2037 LST) 20 March 1995, 2 h after local sunset at 1839 LST. The parameters for this front are listed in Table 2. They include the beginning and end times for the frontal passage; the frontal velocity U_f, as calculated by isochrone analysis of the frontal passage at surface stations in western and central Kansas; the wind shift ΔD from before to after the front; the temperature change ΔT; the mixing ratio change Δq; the time for the frontal zone to pass the tower Δt; and the calculated frontal width Δ. The frontal zone is defined by the beginning and the end of the wind shift associated with the frontal passage, a criterion used, for example, by Taylor et al. (1993).

Time series spanning the period 0000–0600 UTC 20 March 1995 are shown in Fig. 2. The 6-h time period was chosen because it allows time for the front to completely pass the instrumented tower, with time on either side to view the state of the surface layer. The top two panels show wind speed and wind direction from the 10-m south tower sonic anemometer, at a rate of 10 samples per second. The next panel shows dry bulb temperature from the 10-m south tower platinum resistance thermometer, also at 10 samples per second. The last panel shows two surface layer scaling parameters: the local friction velocity u_*, given by

TABLE 2. Parameters for the 20 Mar 1995 cold front.

Begin (UTC)	End (UTC)	U_f (m s^{-1})	ΔD (°)	ΔT (°C)	Δq (g kg^{-1})	Δt (s)	Δ (m)
0237	0312	12	70	−2.5	−3	2100	25 200

$$u_*^2 = \sqrt{\overline{uw}^2 + \overline{vw}^2} \tag{4}$$

(Stull 1988; Garratt 1992), where the momentum fluxes $\overline{uw}$ and $\overline{vw}$ are computed from the 3-m south tower sonic anemometer, and the Monin–Obukhov scaling parameter $\zeta = z/L$, where L is a local Obukhov length, given by

$$L = \frac{-u_*^3 \Theta}{kg\overline{w\theta_v}}. \tag{5}$$

Here, k is the von Kármán constant, with a value of 0.365, g is the gravitational acceleration constant, Θ is the mean potential temperature between 2 and 10 m, and $\overline{w\theta_v}$ is the virtual potential temperature flux calculated from the 3-m sonic anemometer. These scaling parameters are calculated using 900-s averaging intervals, centered on the time of the frontal passage. The dotted lines delimit the frontal zone, as listed in Table 2.

Note, visually, the sharp increase in wind speed variance with the passing of the front. After the front passes, the wind speed and speed variance decay to near-prefrontal values. The wind has a southwesterly component in the prefrontal period. The temperature trace in the third panel shows that there was a 2°C rise in temperature starting at 0200 UTC, possibly due to advection of warmer air from the southwest or increased mixing in the surface layer. After the frontal passage, temperature decreased steadily due to radiational cooling and cold air advection. The wind shift and temperature drop were not coincident in this front, with the temperature drop at 10 m lagging the wind shift by about 180 s. This is also observed in Taylor et al. (1993) and Shapiro et al. (1985), suggesting that this front may have an elevated head, like a density current.

3. Energy and dissipation spectra

According to the universal equilibrium hypothesis of Kolmogorov (1941a, 1962), the dissipative scales of turbulence are statistically independent of the large, energy-containing scales in a fully developed turbulent flow. Under the equilibrium hypothesis, the shape of the normalized spectrum is posited to be a universal function of Reynolds number. The bulk of the data supporting the equilibrium hypothesis were collected in controlled wind tunnel experiments (Comte-Bellot and Corrsin 1965; Champagne 1978; Saddoughi and Veeravalli 1994) or under narrowly specified conditions in the atmospheric boundary layer (Williams and Paulson 1977; Champagne et al. 1977; Champagne 1978; Oncley et al. 1996). The data presented here, on the other hand, were collected in the atmospheric boundary layer during the passage of a sharply defined synoptic-scale cold

front. One-dimensional kinetic energy spectra are calculated as functions of time using data from the sonic and hot-wire anemometers at intervals before, during, and after the frontal passage. These spectra are nondimensionalized with Kolmogorov scales to test for the collapse of the spectra into a dimensionless function that can be compared with the results from the authors cited above.

a. Theoretical and experimental background

Taylor's hypothesis must be invoked to convert the frequency spectra calculated from the sonic and hot-wire anemometer data to the wavenumber domain used in turbulence theory. The appropriate form of Taylor's hypothesis is given by

$$fS_u(f) = \kappa_1 F_{11}(\kappa_1), \tag{6}$$

where f is frequency, $S_u(f)$ is the frequency spectrum of the streamwise velocity component, F_{11} is the one-dimensional streamwise wavenumber spectrum (which is measured by the hot-wire anemometer), and κ_1 is the streamwise wavenumber, related to f by

$$\kappa_1 = \frac{2\pi f}{U}, \tag{7}$$

where U is the advection velocity (Tennekes and Lumley 1972).

Taylor's hypothesis is an approximation. It is valid only when the turbulence intensity in a flow is small, or to first order,

$$\frac{u}{U} \ll 0.1, \tag{8}$$

where u is a characteristic velocity of the turbulent fluctuations (Tennekes and Lumley 1972). This condition is often not met for tower-based turbulence measurements in the atmospheric boundary layer (Wyngaard 1986), including during this frontal passage. For high-intensity turbulence, when (8) is not valid, Lumley (1965) developed a model wherein the advection velocity U in (7) is not constant, but is instead composed of mean and fluctuating components. Wyngaard and Clifford (1977) used Lumley's model to derive a correction for the streamwise wavenumber spectrum F_{11}. In the inertial range, the correction is

$$F_{11}^m = F_{11}\left(1 - \frac{\overline{u^2}}{9U^2} + \frac{2\overline{v^2}}{3U^2} + \frac{2\overline{w^2}}{3U^2}\right), \tag{9}$$

where F_{11}^m denotes the measured wavenumber spectrum; F_{11} is the true spectrum; and the wind speed variances $\overline{u^2}$, $\overline{v^2}$, and $\overline{w^2}$ are computed from time series (Champagne 1978). Champagne (1978) took Lumley's model a step further by actually solving for the true streamwise wavenumber spectrum F_{11} as a function of F_{11}^m and wavenumber κ_1, thereby providing a means of correcting the measured spectrum in both the inertial and dissipative ranges. Wyngaard and Clifford (1977) also give the correction for the streamwise derivative variance

$$\overline{\left(\frac{\partial u}{\partial x}\right)^2}^m = \overline{\left(\frac{\partial u}{\partial x}\right)^2}\left(1 + \frac{\overline{u^2}}{U^2} + 2\frac{\overline{v^2}}{U^2} + 2\frac{\overline{w^2}}{U^2}\right). \tag{10}$$

This correction is used for the direct calculation of dissipation rate (see section 4). This result was also derived independently by Heskestad (1965), under slightly different assumptions.

The scaling relations for the three-dimensional energy spectrum obtained from Kolmogorov's hypotheses hold for the one-dimensional spectrum F_{11} (Hinze 1975). When normalized by Kolmogorov scales, F_{11} takes the form

$$F_{11}(\kappa_1) = \epsilon^{1/4}\nu^{5/4}\varphi_{11}(\eta\kappa_1) \tag{11}$$

in the equilibrium range, where η is given by (2) and $\varphi_{11}(\eta\kappa_1)$ is a universal function of Re_λ. In the inertial subrange, dimensional analysis and isotropy lead to the $-5/3$ law of spectral decay (Hinze 1975)

$$F_{11}(\kappa_1) = \alpha_1\epsilon^{2/3}\kappa_1^{-5/3}, \tag{12}$$

where α_1 is the streamwise Kolmogorov constant. This result is used for the inertial dissipation calculation of dissipation rate (see section 4).

To clearly present changes in the energy spectrum brought about by the frontal passage, spectra from three periods are selected for display:

- an hour before the front, in a developing stable surface layer;
- during the frontal passage;
- an hour after the completion of the frontal passage, when a stable surface layer is redeveloping; z/L is increasing.

The selection of these periods is arbitrary, since there is no theory to guide at what time relative to the front they should be picked. Table 3 summarizes the information used in computing the three spectra. The periods are denoted before (B), during (F), and after (A) the frontal passage. For each period, Table 3 displays mean wind speed U and the component fluctuation wind speeds σ_u, σ_v, and σ_ω, computed from the sonic anemometer. Means are taken over the duration of the 900-s period. Mean dissipation rate ϵ (discussed in section 4), the Kolmogorov microscale η, the Taylor microscale λ, and the turbulence Reynolds number Re_λ are calculated from the high-rate hot-wire data. The Taylor microscale is define here as (Tennekes and Lumley 1972)

$$\lambda = \frac{\sigma_u}{\sigma_{\partial u/\partial x}}, \tag{13}$$

where σ_u and $\sigma_{\partial u/\partial x}$ are the root-mean-square values of the streamwise velocity and the streamwise velocity derivative, respectively. Using the Taylor microscale, a turbulence Reynolds number can be calculated:

TABLE 3. Selection times and turbulence parameters for the three spectra chosen to describe the 20 Mar 1995 front. The statistics are computed at a height of 3 m. See the text for additional details.

Period	Time (UTC)	U (m s^{-1})	σ_u (m s^{-1})	σ_v (m s^{-1})	σ_w (m s^{-1})	ϵ (m^2 s^{-3})	η (mm)	λ (m)	Re_λ	F_{11}^m/F_{11} (IR)	$\overline{u_{1,1}^2}^m/\overline{u_{1,1}^2}$ (DR)
B	0130–0145	3.2	0.55	0.36	0.27	0.027	0.61	0.057	2000	1.010	1.070
F	0245–0300	10.8	2.36	1.52	0.90	0.760	0.27	0.051	8000	1.013	1.106
A	0415–0430	6.3	1.33	0.98	0.54	0.105	0.42	0.055	5000	1.016	1.107

$$\mathrm{Re}_\lambda = \frac{\sigma_u \lambda}{\nu}. \tag{14}$$

Here, the kinematic molecular viscosity ν is considered to be 1.5×10^{-5} m^2 s^{-1}. In the final two columns, two corrections for high-intensity turbulence are calculated, the correction for the one-dimensional spectrum F_{11} in the inertial subrange and the correction for the mean square streamwise velocity derivative $\overline{(\partial u/\partial x)^2}$, which has most of its contributions in the dissipative range. Both corrections are from Wyngaard and Clifford (1977).

b. Kolmogorov spectrum: First moment

Figure 3a shows the three spectra from before, during, and after the frontal passage on 20 March 1995 plotted as dimensionless Kolmogorov spectra $\varphi_{11}(\eta\kappa_1)$. The spectra appear to collapse, as suggested by the universal equilibrium theory, despite the different conditions under which they were measured. Here, three consecutive 300-s wind speed spectra from the hot-wire anemometer in the B, F, and A periods are smoothed by block averaging the spectral estimates in 75 nonoverlapping bands spaced over the logarithm of frequency. This technique is discussed in Blackman and Tukey (1959) and used, for example, in Williams and Paulson (1977). The wind speed spectra are then converted to wavenumber spectra using (6) and made dimensionless using mean values of dissipation rate ϵ and kinematic viscosity ν from the corresponding time intervals according to (11). Note that the value of ϵ calculated using the inertial dissipation technique with the hot-wire anemometer is used, since the direct technique was unusable in high wind speed conditions, as explained in sections 2 and 4. The dotted line shows a negative five-thirds slope indicative of an inertial subrange in the spectrum, according to (12). The noise floor of the hot-wire anemometer, manifested as a flattening of the spectrum at high frequencies, is apparent in the spectra taken in the B and A periods.

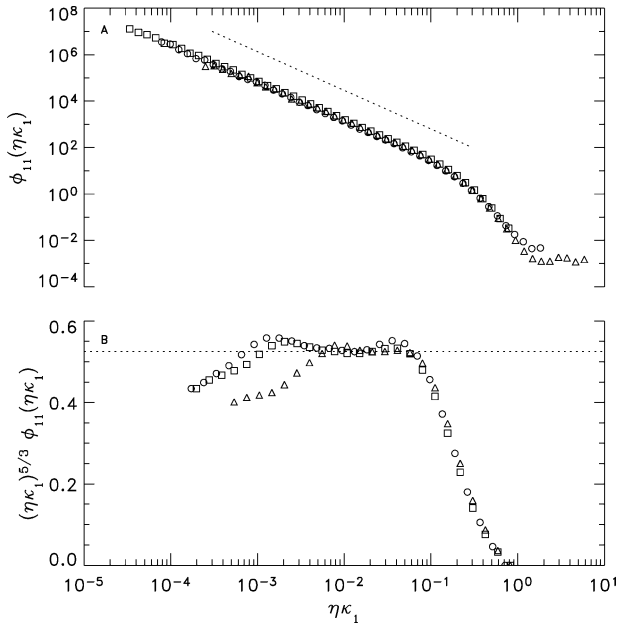

FIG. 3. Universal Kolmogorov spectra plotted vs dimensionless wavenumber $\eta\kappa_1$. Data are from the hot-wire anemometer before (△), during (□), and after (○) the frontal passage. See Table 3 for the time and Re_λ of each spectrum. (a) The first-moment spectrum φ_{11}. The dotted line above the curves denotes a −5/3 slope. (b) The compensated Kolmogorov spectrum $\psi_{11} = (\eta\kappa_1)^{5/3}\varphi_{11}$. The dotted line shows a value of 0.53 for the streamwise Kolmogorov constant α_1.

Figure 3b shows the compensated Kolmogorov spectrum function $\psi_{11} = (\eta\kappa_1)^{5/3}\varphi_{11}$ calculated from the hot-wire anemometer data in the B, F, and A periods of the front. Fifteen compensated spectra computed over consecutive 60-s intervals are interpolated with a cubic spline function to a set of logarithmically spaced abscissas, corresponding to the plotted values of $\eta\kappa_1$. The inertial range correction (9) has been applied to these spectra. The dotted line gives a value of 0.53 for the streamwise Kolmogorov constant α_1 for these data. This value compares well with others in the literature (Wyngaard and Coté 1971; Williams and Paulson 1977; Champagne 1978; Dyer and Hicks 1982; Oncley et al. 1996).

The advantage of the compensated Kolmogorov spectra is that it shows the inertial subrange as a horizontal line, without the distortion of a logarithmic ordinate. The Reynolds number dependence of the three curves is seen as an elongation of the constant level of the inertial subrange. The constant level is small for the B period, but it is longer in the F and A periods, consistent with the larger Re_λ in these regions. This follows from the increasing separation of the energy-containing and dissipative scales with increasing Re_λ. Despite the large Re_λ, the three spectra achieve a nearly constant value over barely 2 decades of normalized wavenumber.

Several authors have commented on the ''bump'' that

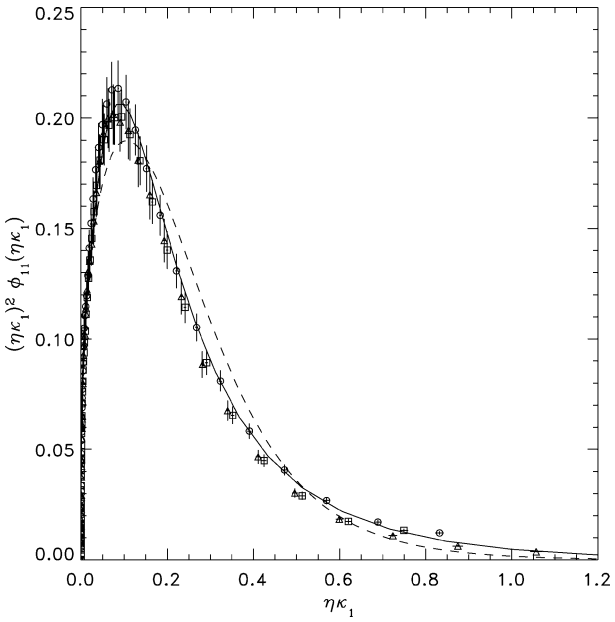

FIG. 4. Kolmogorov second-moment spectra $(\eta\kappa_1)^2\ \varphi_{11}$ plotted vs dimensionless wavenumber $\eta\kappa_1$ on linear axes. Data are from the hot-wire anemometer before (△), during (□), and after (○) the frontal passage. Table 3 gives the time and Re_λ of each spectrum. Crosshairs give 95% confidence intervals for the data values. The solid line gives the curve fit supplied by Champagne (1978) for the normalized spectrum at $\mathrm{Re}_\lambda = 7000$. The dashed line shows the theoretical model spectrum from Pope (2000).

appears in the compensated Kolmogorov spectrum ψ_{11} at normalized wavenumber $\eta\kappa_1 \approx 0.05$. This phenomenon is seen, for example, in the compensated spectra presented by Saddoughi and Veeravalli (1994, Fig. 13), Mestayer (1982, Fig. 10b), and Gotoh et al. (2002). But it may or may not be present in the spectra from Champagne (1978, Fig. 25) or Williams and Paulson (1977, Fig. 6). Sreenivasan and Antonia (1997) call this the bottleneck phenomenon. It is hypothesized that it represents a buildup of excess energy in the inertial range that is waiting to be dissipated. Notice that a secondary bump appears at the low-frequency end of the constant-ψ_{11} range in the three spectra. This secondary bump is also seen in the transverse spectrum in Saddoughi and Veeravalli (1994, Fig. 13) and in the streamwise spectrum in Williams and Paulson (1977, Fig. 6).

c. Kolmogorov spectrum: Second moment

Figure 4 shows the Kolmogorov-normalized second-moment spectrum $(\eta\kappa_1)^2\ \varphi_{11}$ in the B, F, and A periods. The spectra are normalized with Kolmogorov scales and plotted versus normalized frequency. When dimensionalized and integrated, the result is the mean dissipation rate ϵ for each period. Three consecutive 300-s spectra, corrected with the formula provided by Champagne (1978), are composited to form the curves shown in each 900-s interval. Mean values are displayed with symbols, with 95% confidence intervals, based on the variation of ϵ and F_{11}, plotted as crosshairs on the means. The development of the error analysis is covered in Piper (2001). Despite the differences in the spectral amplitudes, Re_λ and ϵ, the spectra collapse. Note, however, that the spectrum taken during the F period does not achieve $\eta\kappa_1 = 1.0$, consistent with the bandwidth limitation of the hot-wire anemometer discussed in section 2.

The eleventh-order polynomial curve fit to the Kolmogorov spectrum supplied by Champagne (1978, his Table 4) is also plotted. It was computed using corrected spectra taken in the atmospheric boundary layer in the Minnesota experiment (Champagne et al. 1977) at $\mathrm{Re}_\lambda = 7000$. The measured spectra here compare favorably with the Champagne data, although there is a discrepancy at the high-wavenumber end of the inertial subrange. The measured spectra also compare well against data from lower Re_λ; see, for example, Fig. 9 from Saddoughi and Veeravalli (1994). Additionally, a theoretical model prediction for the spectrum from Pope (2000) is presented. The model spectrum appears to agree well with the spectra from the present study in the inertial subrange ($\eta\kappa_1 < 0.05$) and at the higher end of the dissipative range ($\eta\kappa_1 > 0.5$), but there is disagreement throughout the rest of the dissipative range.

The value of $\eta\kappa_1$ at which the three spectra reach their maximum value is approximately $\eta\kappa_1 = 0.08$. This compares fairly well with observational data from Grant et al. (1962), Champagne et al. (1977), Williams and Paulson (1977), Champagne (1978), and Saddoughi and Veeravalli (1994). In those studies, the maximum in the second moment spectrum is found consistently at $\eta\kappa_1 \approx 0.1$. Also, the theoretical model of Pope (2000) gives the maximum at $\eta\kappa_1 \approx 0.1$, although it is apparent that the modeled values do not match the Champagne data or the current data very well for $\eta\kappa_1 > 0.05$. The maximum value of $(\eta\kappa_1)^2\ \varphi_{11}$ is between 0.20 and 0.22 for the spectra displayed in Fig. 4. These values compare well with the values given by the authors above (between 0.21 and 0.22), although there is noticeably more scatter here than in the data presented in Champagne (1978, Fig. 22).

TABLE 4. A list of the four techniques used to calculate dissipation rate in this study.

Technique	Instrument	Acronym	Equation
Direct dissipation	Hotwire	HD	(16)
Inertial dissipation	Hotwire	HI	(17)
Kolmogorov's four-fifths law	Hotwire	HK	(19)
Inertial dissipation	Sonic	SI	(17)

4. Dissipation rate

Dissipation rate was measured directly with the hot-wire anemometer and calculated, using two inertial range techniques, with data collected from the sonic and

hot-wire anemometers. For reference, Table 4 provides a list of the calculations. A quantitative comparison between the estimated and directly calculated values of ϵ provides a test of the relative value of the inertial range estimates under varying turbulence and stability conditions.

a. The direct dissipation technique

Under the assumption of local isotropy, since there is no preferred direction, the tensorial form of the mean turbulent kinetic energy dissipation rate ϵ reduces to a form that includes only a single velocity derivative (Tennekes and Lumley 1972):

$$\epsilon = 15\nu\overline{\left(\frac{\partial u}{\partial x}\right)^2}, \tag{15}$$

where ν is the kinematic viscosity, x is in the streamwise direction, and u is the velocity component in that direction.

Applying Taylor's hypothesis with (10), the Heskestad–Lumley correction for high-intensity turbulence, to (15) yields

$$\epsilon = \frac{15\nu}{U^2}\overline{\left(\frac{\partial u}{\partial t}\right)^2}\left(1 + \frac{\overline{u^2}}{U^2} + 2\frac{\overline{v^2} + \overline{w^2}}{U^2}\right)^{-1}. \tag{16}$$

Because velocity derivative terms are involved, the correct instrument to use is the hot-wire anemometer, since it is one of the few instruments capable of resolving the sharp gradients that occur at the smallest scales of turbulent motion. Equation (16) uses the square of the fluctuating wind speed derivative. A derivative series is constructed by differentiating the hot-wire wind speed series U. The derivative series is low-pass filtered at the noise floor of the hot-wire anemometer. The square of the derivative series is then calculated over nonoverlapping 60-s intervals. The terms $\overline{u^2}$, $\overline{v^2}$, $\overline{w^2}$, and U^2 are computed with a 900-s average from the sonic anemometer. The time series of these terms are then interpolated to 60-s intervals for use in (16). The kinematic viscosity ν varies weakly as a function of temperature, so its value is indexed at 60-s intervals with the temperature measured by the hygrothermometer collocated with the hot-wire anemometer at 3 m. The Heskestad–Lumley correction factor in (16) ranged between 5% and 10%, which is comparable in magnitude to that given by Wyngaard and Coté (1971). Direct calculations of ϵ are not possible at all times during the frontal passage, as discussed in section 2. The values of ϵ calculated when wind speeds are above 7 m s^{-1} are still displayed, yet it is noted that they are incorrect because of this systematic error.

b. The inertial dissipation technique

As described, for example, in Champagne et al. (1977), if $S_{u_i}(f)$ is the frequency spectrum of velocity component u_i in the inertial range and α_i is the Kolmogorov constant for the velocity component, the dissipation rate is given by

$$\epsilon = \frac{2\pi}{U}\left[\frac{f^{5/3}S_{u_i}(f)}{\alpha_i}\right]^{3/2}. \tag{17}$$

This technique can be used by any sensor that has a sufficiently high-frequency response to measure velocities in the inertial range (Oncley et al. 1996). Here, wind speed data from the sonic and hot-wire anemometers are used to estimate ϵ with this technique.

Streamwise velocity spectra S_u were computed from the hot-wire anemometer data as a function of frequency f in consecutive 60-s intervals using a fast Fourier transform (FFT). The spectra were smoothed by block averaging spectral amplitudes in 75 nonoverlapping logarithmically distributed bands, giving approximately 10 bands per decade of the spectrum. Before computing the FFT, the 60-s sample was tapered using a Hamming window. This technique is recommended by Kaimal and Kristensen (1991) to reduce the overestimation of the amplitude of the inertial subrange when using an averaging interval less than the integral time scale of the turbulence being measured. To compensate for the Hamming window, the resulting spectra were multiplied by a factor of 2.52. The average value of $f^{5/3}S_u(f)$ was then computed over the frequency band $5 < f < 30$ Hz. By examination of several hours of frequency spectra, this frequency band was determined empirically to contain a subset of the frequencies where power-law behavior develops in the streamwise velocity spectrum. Mean wind speed U is computed over 900-s intervals, then interpolated to the 60-s intervals. Based on an analysis similar to what produced Fig. 3, a Kolmogorov constant of $\alpha_1 = 0.53$ was chosen for use in (17). This value falls within the distribution of Kolmogorov constants reported in the literature (Wyngaard and Coté 1971; Williams and Paulson 1977; Champagne 1978; Dyer and Hicks 1982; Oncley et al. 1996).

Sonic anemometers measure the u, v, and w components of the wind, with the spectrum of each component obeying (17). Only the streamwise velocity component u is used here, however, because it achieves an inertial subrange first (Kaimal et al. 1972; also see Fig. 1) and because it is contaminated least by probe-induced distortion for our wind data. Spectra of the streamwise velocity component S_u were computed in 60-s intervals, with a Hamming window applied as described above. Following the procedure described in Oncley et al. (1996), $f^{5/3}S_u(f)$ was computed over the frequency band $0.5 < f < 2$ Hz. These bounds were chosen empirically by examining several hours of data; they also are close to the range 0.5–5 Hz used in Wyngaard and Coté (1971) and Oncley et al. (1996). The upper bound at 2 Hz was chosen below the Nyquist frequency of the sonic anemometers, thereby limiting the influence of line averaging on the calculation. The frequency band

where $f^{5/3}S_u(f)$ achieved a maximum, as well as the two adjacent frequency bands, were used to compute a mean value of $f^{5/3}S_u(f)$, which was used in (17). The mean wind speed U was interpolated from the 900-s average value, and a Kolmogorov constant of $\alpha_1 = 0.53$ was used.

c. Kolmogorov's four-fifths law

Another method for calculating dissipation rate is Kolmogorov's four-fifths law, an exact relation derived directly from the Navier–Stokes equations using the assumptions of homogeneity and isotropy. The four-fifths law is given by

$$\overline{\Delta u^3} = \overline{[u(x + r) - u(x)]^3} = -\frac{4}{5}\epsilon r \qquad (18)$$

(Kolmogorov 1941b), where the left-hand side is the third-order streamwise velocity structure function, with the condition that the separation distance r must lie in the inertial subrange.

The four-fifths law gives an appealing method for estimating dissipation rate because there are no undetermined coefficients, unlike (17). The four-fifths law has been studied recently by Praskovsky (1992) and Dhruva et al. (1997), and used in Katul et al. (1994) and Albertson et al. (1997). Sreenivasan and Antonia (1997) suggest that the four-fifths law may provide a less ambiguous estimate of ϵ than the direct method (15), and that it can also be used to fix the extent of the inertial subrange. Dhruva et al. (1997) assert that the four-fifths law appears to hold even in inhomogeneous turbulence.

Taylor's hypothesis is used to convert (18) to the time domain. If $r = U\tau$, where U is mean wind speed and τ is a displacement in time, then (18) can be rearranged to provide a formula for ϵ:

$$\epsilon = -\frac{5}{4}\left(\frac{1}{U\tau}\right)\overline{\Delta u^3}, \qquad (19)$$

with the stipulation now that the separation distance $U\tau$ must fall within the inertial subrange of scales. There is no high-intensity turbulence correction to Taylor's hypothesis for the third-order structure function (Hill 1996). Figure 1 suggests that the sonic anemometers used in the MICROFRONTS experiment do not have the frequency response necessary to use Kolmogorov's four-fifths law to calculate dissipation rate, since the four-fifths law technique requires measurements in the inertial subrange, and evidence of an inertial subrange in the 3-m sonic data is tenuous. The hot-wire anemometer can, however, measure velocities in the inertial range, so data from each are used with (19). Estimates of ϵ using (19) were made in 60-s intervals with the hot-wire anemometer data. The value of r was chosen to be 0.03 m. For the range of U values during the fronts, this choice of r gives values of $f = \tau^{-1}$ that fall within the frequency response of the hot-wire anemometer. The 900-s average value of U was interpolated to the 60-s intervals used to compute ϵ.

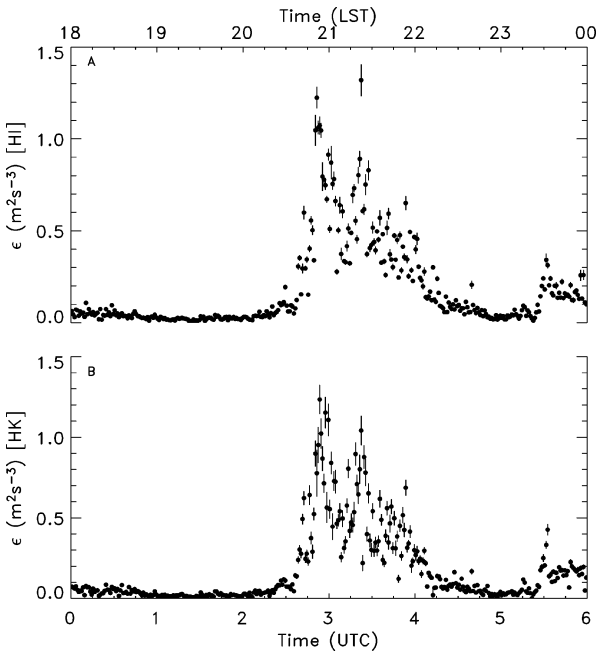

FIG. 5. Dissipation rate calculations from the 3-m hot-wire anemometer for the 20 Mar 1995 front. Values of ϵ are calculated in 60-s intervals. Error bars denote 95% confidence intervals on the means. (a) Inertial dissipation technique (HI). (b) Kolmogorov's four-fifths law (HK).

d. Dissipation rate calculations

Figure 5 shows the inertial dissipation calculation (17) and the calculation from Kolmogorov's four-fifths law (19) using data from the hot-wire anemometer for the 6-h analysis period surrounding the frontal passage. Hereafter, these calculations are referred to as HI and HK, respectively; see also Table 4 for reference. Figure 6 shows the direct dissipation calculation (16) using data from the hot-wire anemometer (HD) and the inertial dissipation calculation using data from the 3-m sonic anemometer (SI) for the same period. Error bars depict 95% confidence intervals on each value of ϵ; see Piper (2001) for a treatment of the error analysis. These figures show that there is an order of magnitude increase in ϵ with this frontal passage. Also, there is fidelity between the four ϵ calculations, even though the direct method (HD) was untenable in high wind speed conditions. Note that the inertial dissipation technique from the sonic anemometer gives reasonable values for ϵ, even though, from Fig. 1, an inertial range is not technically achieved. Here, we are taking advantage of the observation that the streamwise velocity spectrum often displays $-5/3$ power-law behavior outside of the range defined to be the inertial range on the basis of local isotropy (Champagne 1978; Mestayer 1982). This ob-

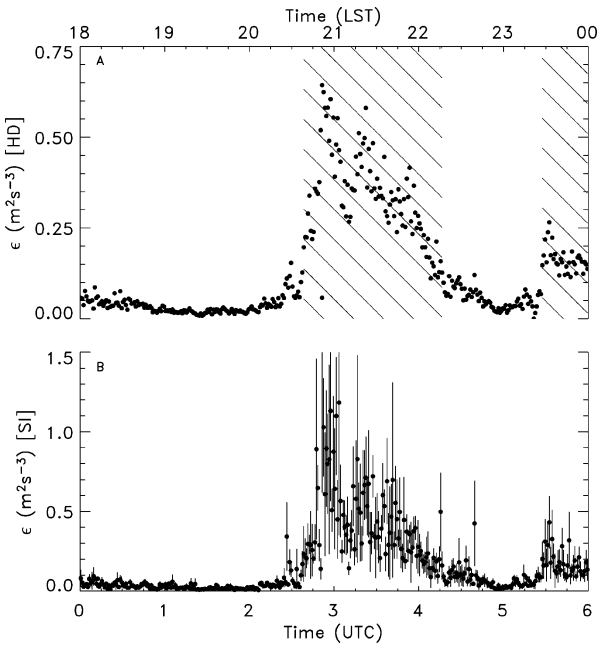

FIG. 6. Dissipation rate calculations from the 3-m hot-wire and sonic anemometers for the 20 Mar 1995 front. Values of ϵ are calculated in 60-s intervals. Error bars denote 95% confidence intervals on the means. (a) Direct dissipation technique from the hot wire (HD). Note the expanded ordinate. The error bars are smaller than the plot symbols. The hatched areas indicate when $U > 7$ m s^{-1}. (b) Inertial dissipation technique from the sonic (SI).

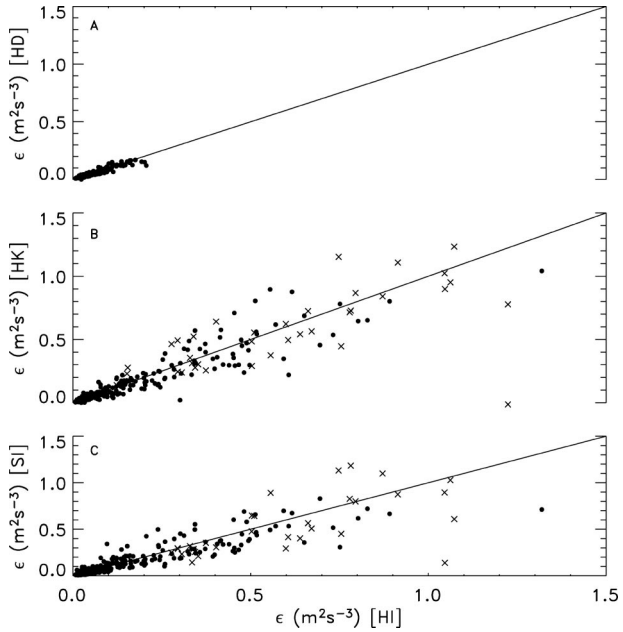

FIG. 7. Scatterplots of the 60-s ϵ calculations for the 20 Mar 1995 front. Symbols refer to calculations made within the frontal zone ($\times$) and before and after the front ($\bullet$). The solid lines show a 1:1 correspondence in the ϵ values. (a) Comparison between inertial dissipation (HI) and direct dissipation (HD) calculations from the hot-wire anemometer. The comparison is only made for wind speeds $U < 7$ m s^{-1}. (b) Comparison between inertial dissipation (HI) and Kolmogorov's four-fifths law (HK) calculations from the hot-wire anemometer. (c) Comparison between inertial dissipation calculations from the hot-wire (HI) and sonic (SI) anemometers.

servation is also used explicitly, for example, in Louis et al. (1983) and Albertson et al. (1997).

The confidence intervals for the HI and HK calculations displayed in Fig. 5 are small, even during the frontal passage, indicating random errors are controlled well. The confidence intervals on the HD calculation are smaller than the plot symbols because of the large number of points used in the calculation in comparison to the tiny integral scales (on the order of the Kolmogorov time scale τ) of the velocity derivative. The confidence intervals on the SI calculation are uncomfortably large. The confidence in these ϵ values could be increased by further averaging in time or by including more points in the average through more spectral bands. Another means by which the confidence could be increased is by including independent calculations of ϵ from the transverse velocity component of the sonic anemometer. However, Kaimal et al. (1972) show that the transverse component does not display $-5/3$ power-law behavior for frequencies as low as those in the streamwise spectrum. Because the SI calculation is made under tenuous evidence of an inertial subrange within the bandwidth capabilities of the 3-m sonic anemometer, the chances of obtaining inertial subrange estimates of ϵ from the transverse velocity component are not good.

Ideally, the four calculations of ϵ (HD, HI, HK, and SI) should yield the same value for the dissipation rate in each 60-s time interval. However, due to systematic errors—for example, the hot-wire frequency response limit in the HD calculation or the lack of true inertial subrange measurements in SI—and random errors, the four calculations do not give the same value in each interval. Figure 7 shows scatterplots comparing the values of ϵ calculated with the four techniques over the 6-h period. In each panel, the 1:1 line is used instead of a least-squares line of regression because none of the ϵ calculations can be considered independent for the purposes of regression. The 1:1 line gives the ideal limit of where the individual data points should lie on each scatterplot. The idea of neutral regression, when neither variable is independent, is discussed in Emery and Thomson (1997). Because the HD method cannot be used in the front, HI is used instead for a basis of comparison with the other calculations. Figure 7 shows that the values of HK and SI are visibly well correlated with the values of HI, as evidenced by the agreement with the 1:1 line in each plot. The agreement is favorable even during the frontal passage. The scatter between the calculations tends to increase with increasing ϵ. The scatter between the methods is mostly due to random error, since increasing the averaging interval reduces the amount of scatter.

Table 5 shows the cross-correlation coefficient ρ and

TABLE 5. A matrix of correlation coefficients ρ and neutral regression error e_r for the four dissipation rate calculations. Comparisons are for the 6-h analysis period ($N = 360$ values) and for the 35-min frontal zone ($N = 35$ values). The HD comparison is made only when $U < 7$ m s^{-1}.

Techniques	N	ρ	e_r
HI–HD	242	0.95	0.13
HI–HK	360	0.94	0.20
	35	0.85	0.19
HI–SI	360	0.89	0.26
	35	0.73	0.23

neutral regression error e_r between each ϵ calculation. Values are displayed for the 6-h analysis period ($N = 360$ points) and for the 35-min frontal zone ($N = 35$ points), with the exception of the HI–HD comparison, which is only shown when $U < 7$ m s^{-1}. The cross-correlation coefficients achieve their maximum at a lag of 0 s. The neutral regression errors represent the mean value of the set of distances of each point in Fig. 7 from the 1:1 line, with each value normalized by the mean value of the two ϵ values being compared. This corresponds to

$$e_r = e_{AB} = \frac{2}{N}\sum_{i=0}^{N-1}\frac{|\epsilon_{Ai} - \epsilon_{Bi}|}{\epsilon_{Ai} + \epsilon_{Bi}}, \tag{20}$$

where A and B represent any two of the methods (HD, HI, HK, or SI) used to calculate ϵ.

The values of the parameters shown in Table 5 suggest that there is a high degree of correlation between the three calculations. The highest degree of correlation is between the calculations made with the hot-wire anemometer, presumably because the bounty of inertial range measurements from the hot wire tend to reduce random errors. The inertial dissipation method from the sonic anemometer also compares fairly well with the hot-wire anemometer calculations. This result is important because it shows that ϵ calculations can be made with a sonic anemometer that compare favorably with those made from a hot-wire anemometer, and sonic anemometers are much sturdier and easier to use and maintain in the field (Oncley et al. 1996).

A larger question is how well do the ϵ calculations compare within the frontal zone? This frontal zone took 35 min to pass the MICROFRONTS site. The three calculations that use hot-wire anemometer data are still well correlated with each other, although their maximum correlation values have decreased due to scatter, since only $N = 35$ calculations are used in the computation of the cross-correlation coefficients. The correlation between the hot-wire calculations and the sonic inertial dissipation calculation has dropped, although the value of the correlation is still reasonably high. This suggests that ϵ calculations from the sonic anemometer can be used when data from the hot-wire anemometer are not available, and that the ϵ values from the sonic will be fairly reliable, even in frontal situations.

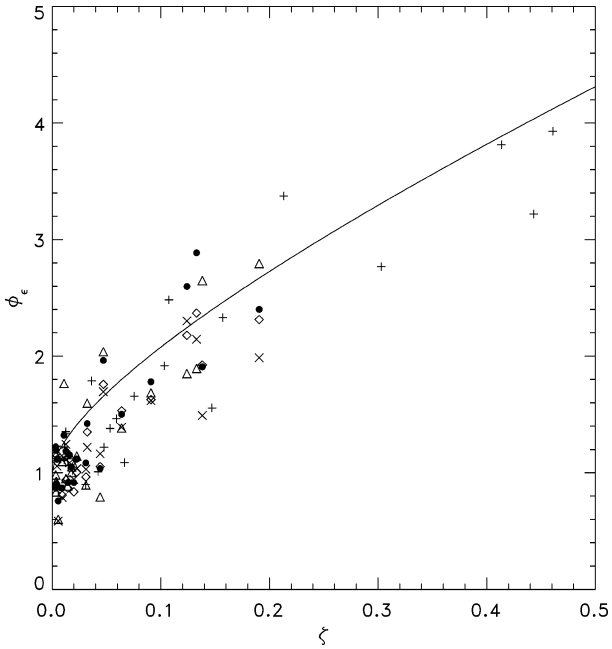

FIG. 8. Dimensionless dissipation rate ϕ_ϵ plotted against the Monin–Obukhov scaling parameter ζ for the dissipation rate calculations made in the 6-h period surrounding the 20 Mar 1995 front. Plot symbols correspond to HD (◇), HI (●), HK (×), SI 3 m (△), and SI 10 m (+). The curve is suggested by Wyngaard and Coté (1971).

e. Normalized dissipation rate

Dissipation rate can be normalized with Monin–Obukhov surface layer similarity scales. The normalized dissipation rate ϕ_ϵ is given by

$$\phi_\epsilon = \frac{kz\epsilon}{u_*^3}, \tag{21}$$

(Wyngaard and Coté 1971), where k is the von Kármán constant, z is the height above the surface, and u_* is the friction velocity. The dimensionless dissipation rate ϕ_ϵ is hypothesized to be a universal function of $\zeta = z/L$, where L is the Obukhov length. Because ϕ_ϵ is expected to be a universal function, it provides a good way to compare the ϵ values calculated here with other ϵ values presented in the literature.

Dimensionless dissipation rate calculations are presented in Fig. 8. Data from the 3-m hot-wire and the 3- and 10-m south tower sonic anemometers are displayed, using all available methods. The dissipation rate calculations are averaged into the 900-s intervals used to calculate u_* and L. Each point therefore corresponds to an average of 15 of the 60-s ϵ calculations displayed in Figs. 5 and 6. A value of $k = 0.365$ was used for the von Kármán constant (Oncley et al. 1996). The line represents the curve fit suggested by Wyngaard and Coté (1971):

$$\phi_\epsilon = (1 + 2.5\zeta^{3/5})^{3/2}. \tag{22}$$

In the previous section, the methods used to calculate ϵ were shown to agree well with one another, indicating a fair degree of precision in the calculations. Figure 8 shows that the ϵ calculations were also fairly accurate, given that they collapse well when normalized with surface layer scales and the normalized values compare favorably with an accepted ϕ_ϵ curve fit. The dimensionless ϵ data are slightly lower in magnitude than the curve fit predicts over the range of ζ displayed. Oncley et al. (1996) also found that their ϵ data near $\zeta = 0$ in stable conditions were smaller than the values predicted by the Wyngaard and Coté curve fit. Similar scatter is found by other researchers (see, e.g., discussion in Oncley et al. 1996).

5. Discussion

Ground truth has been established for turbulence levels within a surface frontal transition zone, including measurements of Kolmogorov spectra and turbulent kinetic energy dissipation rate. These results can be used in assessing the effects of friction in the surface layer in traditional semigeostrophic models of frontal collapse (Hoskins and Bretherton 1972; Williams 1974), or in models with an ageostrophic feedback mechanism (Orlanski and Ross 1984).

Examination of energy spectra shows that the fine scales of turbulence obey Kolmogorov scaling, even when the large scales are subjected to the substantial anisotropic and nonstationary forcing of a cold front. The data quality is high enough to permit testing of the first and second moments of the normalized spectrum. They are found to agree with field data from other experiments. The normalized spectrum is also compared with a recent theoretical model of the equilibrium range proposed by Pope (2000). The theoretical model does not agree particularly well with the current data or the other experimental data through the dissipative range of scales, on the range $0.1 < \eta\kappa_1 < 1.0$.

Direct and indirect methods for calculating dissipation rate are used on data collected before, during, and after the passage of a cold front. Both sonic and hot-wire anemometers are utilized. The calculations from the direct and indirect methods are found to compare well, even though information from different scales of turbulence are used in the calculations, and despite the fact that the calculations are obtained using wind field measurements from different instruments. The agreement in the calculations suggests that the indirect methods can be used safely to calculate ϵ at other height levels where only one turbulence sensor is located, and with data from other fronts, where no direct calculations of ϵ are available. The dissipation rate in the surface layer is found to increase by an order of magnitude in the 20 March 1995 frontal passage to a maximum value of $\sim 1.2\ m^2\ s^{-3}$, compared to prefrontal values of $\sim 0.05\ m^2\ s^{-3}$. Dissipation rate levels remain high even after the passage of the frontal zone. When normalized by Monin–Obukhov surface layer scales, the dissipation rate values agree well with a curve fit proposed by Wyngaard and Coté (1971).

The results of this study may have some immediate utility. For example, information on how the surface layer interacts with fronts and density currents can be useful for pollutant dispersion prediction (Yee et al. 1998; Reitebuch et al. 2000). Additionally, accurate observations of dissipation rate will assist in the modeling of the stably stratified boundary layer (Kosović and Curry 2000).

Acknowledgments. We are indebted to our advisor Bill Blumen, for his guidance and support in science and in life.

Support for MP has been provided by the Air Force Office of Scientific Research under Grant F49620-95-1-014-1 and under AASERT Grant F49620-97-1-0448. Support for MP and JKL at the University of Colorado has been provided by the Atmospheric Sciences Division, Mesoscale Dynamics Program of the National Science Foundation under Grant ATM-9903645. MP also thanks Research Systems, Inc., for allowing a leave of absence.

This work was performed under the auspices of the U.S. Department of Energy by the University of California, Lawrence Livermore National Laboratory under Contract W-7405-Eng-48.

REFERENCES

Albertson, J. D., M. B. Parlange, G. Kiely, and W. E. Eichinger, 1997: The average dissipation rate of turbulent kinetic energy in the neutral and unstable atmospheric surface layer. *J. Geophys. Res.*, **102,** 13 423–13 432.

Blackman, R. B., and J. W. Tukey, 1959: *The Measurement of Power Spectra.* Dover, 190 pp.

Blumen, W., and M. Piper, 1999: The frontal width problem. *J. Atmos. Sci.,* **56,** 3167–3172.

Bruun, H. H., 1995: *Hot-Wire Anemometry.* Oxford University Press, 507 pp.

Champagne, F. H., 1978: The finescale structure of the turbulent velocity field. *J. Fluid Mech.,* **86,** 67–108.

——, C. A. Friehe, J. C. LaRue, and J. C. Wyngaard, 1977: Flux measurements, flux estimation techniques, and finescale turbulence measurements in the unstable surface layer over land. *J. Atmos. Sci.,* **34,** 515–530.

Chapman, D., and K. A. Browning, 2001: Measurements of dissipation rate in frontal zones. *Quart. J. Roy. Meteor. Soc.,* **127,** 1939–1959.

Comte-Bellot, G., and S. Corrsin, 1965: The use of a contraction to improve the isotropy of grid-generated turbulence. *J. Fluid Mech.,* **25,** 657–682.

Dhruva, B., Y. Tsuji, and K. R. Sreenivasan, 1997: Transverse structure functions in high-Reynolds-number turbulence. *Phys. Rev.,* **56I,** R4298–R4930.

Dyer, A. J., and B. B. Hicks, 1982: Kolmogorov constants at the 1976 ITCE. *Bound.-Layer Meteor.,* **22,** 137–150.

Emanuel, K. A., 1985: What limits frontal formation? *Nature,* **315,** 99.

Emery, W. J., and R. E. Thomson, 1997: *Data Analysis Methods in Physical Oceanography.* Pergamon Press, 634 pp.

Frank, H. P., 1994: Boundary layer structure in two fronts passing a tower. *Meteor. Atmos. Phys.,* **53,** 95–109.

Friehe, C. A., 1986: Finescale measurements of velocity, temperature and humidity in the atmospheric boundary layer. *Probing the Atmospheric Boundary Layer*, D. H. Lenschow, Ed., Amer. Meteor. Soc., 269 pp.

Gall, R. L., R. T. Williams, and T. L. Clark, 1987: On the minimum scale of surface fronts. *J. Atmos. Sci.,* **44,** 2562–2574.

Garner, S. T., 1989: Fully Lagrangian numerical solution of unbalanced frontogenesis and frontal collapse. *J. Atmos. Sci.,* **46,** 717–739.

Garratt, J. R., 1992: *The Atmospheric Boundary Layer*. Cambridge University Press, 316 pp.

Gotoh, T., D. Fukuyama, and T. Nakano, 2002: Velocity field statistics in homogeneous steady turbulence obtained using a high-resolution direct numerical simulation. *Phys. Fluids,* **14,** 1065–1081.

Grant, H. L., R. W. Stewart, and A. Moilliet, 1962: Turbulent spectra from a tidal channel. *J. Fluid Mech.,* **12,** 241–268.

Heskestad, G., 1965: A generalized Taylor hypothesis with application for high Reynolds number turbulent shear flows. *J. Appl. Mech.,* **3,** 735–739.

Hill, R. J., 1996: Corrections to Taylor's frozen turbulence approximation. *Atmos. Res.,* **40,** 153–175.

Hinze, J. O., 1975: *Turbulence.* 2d ed. McGraw-Hill, 790 pp.

Hoskins, B. J., and F. P. Bretherton, 1972: Atmospheric frontogenesis models: Mathematical formulation and solutions. *J. Atmos. Sci.,* **29,** 11–37.

Kaimal, J. C., 1986: Flux and profile measurements from towers in the boundary layer. *Probing the Atmospheric Boundary Layer*, D. H. Lenschow, Ed., Amer. Meteor. Soc., 269 pp.

——, and L. Kristensen, 1991: Time series tapering for short data samples. *Bound.-Layer Meteor.,* **57,** 187–194.

——, J. C. Wyngaard, Y. Izumi, and O. R. Coté, 1972: Spectral characteristics of surface layer turbulence. *Quart. J. Roy. Meteor. Soc.,* **98,** 563–589.

Katul, G. G., M. B. Parlange, and C. R. Chu, 1994: Intermittency, local isotropy and non-Gaussian statistics in atmospheric surface layer turbulence. *Phys. Fluids,* **6,** 2480–2492.

Kennedy, P. J., and M. A. Shapiro, 1975: The energy budget in a clear air turbulence zone as observed by aircraft. *Mon. Wea. Rev.,* **103,** 650–654.

Kolmogorov, A., 1941a: The local structure of turbulence in incompressible viscous fluid for very large Reynolds numbers. *Dokl. Akad. Nauk SSSR,* **30,** 9–13. [Reprinted as Kolmogorov, A., 1991: The local structure of turbulence in incompressible viscous fluid for very large Reynolds numbers. *Proc. Roy. Soc.*, **434A**, 9–13.]

——, 1941b: Dissipation of energy in locally isotropic turbulence. *Dokl. Akad. Nauk SSSR,* **32,** 16–18. [Reprinted as Kolmogorov, A. N., 1991: Dissipation of energy in locally isotropic turbulence. *Proc. Roy. Soc.*, **434A,** 15–17.]

——, 1962: A refinement of the previous hypotheses concerning the local structure of turbulence in a viscous incompressible fluid at high Reynolds number. *J. Fluid Mech.,* **13,** 82–85.

Kosović, B., and J. A. Curry, 2000: A large eddy simulation study of a quasi-steady, stably stratified atmospheric boundary layer. *J. Atmos. Sci.,* **57,** 1052–1068.

Louis, J. F., A. Weill, and D. Vidal-Madjar, 1983: Dissipation length in stable layers. *Bound.-Layer Meteor.,* **25,** 229–243.

Lumley, J. L., 1965: Interpretation of time spectra measured in high intensity shear flows. *Phys. Fluids,* **8,** 1056–1062.

Mestayer, P. G., 1982: Local isotropy and anisotropy in a high-Reynolds-number turbulent boundary layer. *J. Fluid Mech.,* **125,** 475–503.

Oncley, S. P., C. A. Friehe, J. A. Businger, E. C. Itsweire, J. C. LaRue, and S. S. Chang, 1996: Surface layer fluxes, profiles and turbulence measurements over uniform terrain under near-neutral conditions. *J. Atmos. Sci.,* **53,** 1029–1044.

Orlanski, I., and B. B. Ross, 1984: The evolution of an observed cold front. Part II: Mesoscale dynamics. *J. Atmos. Sci.,* **41,** 1669–1703.

——, ——, L. Palinsky, and R. Shaginaw, 1985: Advances in the theory of atmospheric fronts. *Adv. Geophys.,* **27,** 223–252.

Piper, M., 2001: The effects of a frontal passage on finescale nocturnal boundary layer turbulence. Ph.D. thesis, University of Colorado, Boulder, 217 pp.

Pope, S. B., 2000: *Turbulent Flows.* Cambridge University Press, 771 pp.

Praskovsky, A., 1992: Experimental verification of the Kolmogorov refined similarity hypothesis. *Phys. Fluids,* **4A,** 2589–2591.

Reitebuch, O., A. Strassburger, S. Emeis, and W. Kuttler, 2000: Nocturnal secondary ozone concentration maxima analysed by sodar observations and surface measurements. *Atmos. Environ.,* **34,** 4315–4329.

Saddoughi, S. G., and S. V. Veeravalli, 1994: Local isotropy in turbulent boundary layers at high Reynolds number. *J. Fluid Mech.,* **268,** 333–372.

Shapiro, M. A., 1984: Meteorological tower measurements of a surface cold front. *Mon. Wea. Rev.,* **112,** 1634–1639.

——, T. Hampel, D. Rotzoll, and F. Mosher, 1985: The frontal hydraulic head: A micro-α scale ($\sim$1 km) triggering mechanism for mesoconvective weather systems. *Mon. Wea. Rev.,* **113,** 1166–1183.

Snyder, C., W. C. Skamarock, and R. Rotunno, 1993: Frontal dynamics near and following frontal collapse. *J. Atmos. Sci.,* **50,** 3194–3211.

Sreenivasan, K. R., and R. Antonia, 1997: The phenomenology of small-scale turbulence. *Annu. Rev. Fluid Mech.,* **29,** 435–472.

Stull, R. B., 1988: *An Introduction to Boundary Layer Meteorology.* Kluwer Academic, 666 pp.

Taylor, P. A., J. R. Salmon, and R. E. Stewart, 1993: Mesoscale observations of surface fronts and low pressure centres in Canadian East Coast storms. *Bound.-Layer Meteor.,* **64,** 15–54.

Tennekes, H., and J. L. Lumley, 1972: *A First Course in Turbulence.* The MIT Press, 300 pp.

Williams, R. M., and C. A. Paulson, 1977: Microscale temperature and velocity spectra in the atmospheric surface layer. *J. Fluid Mech.,* **83,** 547–567.

Williams, R. T., 1974: Numerical simulation of steady-state fronts. *J. Atmos. Sci.,* **31,** 1286–1296.

Wyngaard, J. C., 1986: Measurement physics. *Probing the Atmospheric Boundary Layer*, D. H. Lenschow, Ed., Amer. Meteor. Soc., 269 pp.

——, and O. R. Coté, 1971: The budgets of turbulent kinetic energy and temperature variance in the surface layer. *J. Atmos. Sci.,* **28,** 190–201.

——, and S. F. Clifford, 1977: Taylor's hypothesis and high-frequency turbulence spectra. *J. Atmos. Sci.,* **34,** 922–929.

Yee, E., P. R. Kosteniuk, and J. F. Bowers, 1998: A study of concentration fluctuations in instantaneous clouds dispersing in the atmospheric surface layer for relative turbulent diffusion: Basic descriptive statistics. *Bound.-Layer Meteor.,* **87,** 409–457.

Young, G. S., and R. H. Johnson, 1984: Meso- and microscale features of a Colorado cold front. *J. Climate Appl. Meteor.,* **23,** 1315–1325.